

PAPER • OPEN ACCESS

## Subaperture stitching wavelength scanning interferometry for 3D surface measurement of complex-shaped optics

To cite this article: Yong Bum Seo *et al* 2021 *Meas. Sci. Technol.* **32** 045201

View the [article online](#) for updates and enhancements.

### You may also like

- [Astigmatism correction of convex aspheres using the subaperture stitching hindle test](#)  
Goeun Kim, In-Ung Song, Hagyong Kihm et al.
- [Adaptive Optics Sky Coverage Calculations for the GeminiNorth Telescope](#)  
B. L. Ellerbroek and D. W. Tyler
- [Measurement of aspheric surfaces using an improved annular subaperture stitching interferometry \(IASSI\)](#)  
Yongfu Wen and Haobo Cheng

# Subaperture stitching wavelength scanning interferometry for 3D surface measurement of complex-shaped optics

Yong Bum Seo<sup>1,2</sup>, Ki-Nam Joo<sup>3</sup> , Young-Sik Ghim<sup>1,2</sup>  and Hyug-Gyo Rhee<sup>1,2</sup>

<sup>1</sup> Optical Imaging and Metrology Team, Advanced Instrumentation Institute, Korea Research Institute of Standards and Science (KRISS), Science Town, Daejeon 34113, Republic of Korea

<sup>2</sup> Department of Science of Measurement, University of Science and Technology (UST), Science Town, Daejeon 34113, Republic of Korea

<sup>3</sup> Department of Photonic Engineering, Chosun University, 309 Pilmun-daero, Dong-gu, Gwangju 61452, Republic of Korea

E-mail: [young.ghim@kriss.re.kr](mailto:young.ghim@kriss.re.kr) and [hrhee@kriss.re.kr](mailto:hrhee@kriss.re.kr)

Received 21 July 2020, revised 26 November 2020

Accepted for publication 3 December 2020

Published 10 February 2021



## Abstract

Subaperture stitching wavelength scanning interferometry with a high-accuracy multi-axis position stage is proposed for measuring complex surface shapes such as aspherical and freeform optics. Typical optical approaches suffer due to poor fringe visibility when it comes to complex-shaped optics. Our proposed technique allows a proper solution to this challenging issue by keeping the optical probe perpendicular to the surface slope, which provides good fringe visibility during the wavelength scan regardless of how steep the surface is. Also, the full-aperture surface map of a test sample can be obtained by stitching multiple subaperture measurement results with high precision. We tested and verified our method by measuring several representative samples and comparing the measurement results with a well-established stylus method.

Keywords: subaperture stitching wavelength scanning interferometry, complex shape optics, 3D surface measurement

(Some figures may appear in colour only in the online journal)

## 1. Introduction

In recent years, freeform optics have emerged as the next generation optical components by providing an efficient and aesthetic design, as well as superior optical performance, with fewer elements compared to conventional rotationally symmetric optics. For these reasons, freeform optics have been widely adopted at a rapid rate and have become significant

optical components across high-tech industries in applications such as head-mounted displays, high-resolution imaging systems, and smartglasses [1, 2]. However, many obstacles and barriers still remain in ensuring quality control during the mass production of freeform optics with nonrotationally symmetric features.

To ensure the product will meet its requirements, a reliable measurement method is needed. In many metrology solutions, the most intuitive approach is a point contact method with a stylus. As a representative point-by-point method, the ultra-highly accurate 3D profilometer (UA3P) is capable of measuring any freeform surface with nanometer precision [3]. But 3D measurement is time consuming and there is a risk of sample damage. Given the above problems, optical noncontact approaches can be alternative solutions.



Original content from this work may be used under the terms of the [Creative Commons Attribution 4.0 licence](https://creativecommons.org/licenses/by/4.0/). Any further distribution of this work must maintain attribution to the author(s) and the title of the work, journal citation and DOI.

Generally, optical-based methods can be categorized as either a slope-measuring technique [4–9] or a surface-measuring technique [10–15]. The slope measuring methods such as lateral shearing interferometry [4, 5] and deflectometry [6, 7] fundamentally measure the slope profile itself. And then the height profile is reconstructed through integration [8, 9]. This slope-measuring technique offers significant advantages for 3D measurements of complex shapes such as freeform optical surfaces, since it requires no reference and provides a large dynamic range. However, it needs relatively complicated calibration for surface reconstruction and the errors in the slope measurement will significantly propagate into the resultant surface profile.

On the other hand, surface-measuring techniques, such as phase shifting interferometry [10–12] and coherence scanning interferometry [13–15], measure the surface profile directly by converting the phase information into the surface height. So the calibration work is not tricky and complex compared to slope-measuring techniques. But the surface-measuring approach has difficulties with measurements due to poor fringe visibility or too dense fringe patterns because the optical path difference (OPD) between the reference and the measurement increases considerably when it comes to complex shape measurements [16].

Recently, LuphoScan [17] and NANOMEFOS [18] have shown remarkable progress as point-cloud optical metrology solutions for the 3D measurement of complex surface shapes with high accuracy, but these point-by-point methods are relatively time-consuming and require many expensive sensors with high accuracy. To overcome these technical limitations, we propose a subaperture stitching wavelength scanning interferometry, for full coverage measurement of complex-shaped optics. A wavelength tunable laser is used to minimize the mechanical error sources due to moving parts during the measurement [19–21]. To obtain good visibility of the fringe pattern even for freeform surfaces, we keep the optical probe perpendicular to the surface slope and obtain good quality coverage of fringes during the wavelength scan using high accuracy multi-axis position stage. Here, the surface slope for each measurement is calculated in advance from the surface equation provided by the manufacturer. Based on this information, we control the multi-axis position stage to obtain the best visibility of fringe patterns by maintaining the perpendicular geometrical relation between the optical probe and the surface. Then, the full-aperture surface map is reconstructed by combining or stitching together multiple subaperture maps [22–24].

## 2. Subaperture stitching wavelength scanning interferometry

Figure 1 shows a schematic diagram of our proposed method. The rotating ground glass diffuser (RGGD) is placed near the focal point of the illumination optics to reduce speckle noise, and a beam passing through the illumination optics is reflected from the beam splitter (BS). Then, this reflected beam enters the Michelson-type interferometric objectives (MIO)

and is divided into the reference beam and the measurement beam, respectively. Here, the illumination optics is designed as Köhler illumination to provide a uniformly illuminated field of view of the target and the reference mirror at the same time. In the MIO, the two reflected beams from the reference flat and the measurement target are recombined. Then an interference pattern is created and delivered to a charge coupled device (CCD) camera for data processing via imaging optics. Here, the OPD between the measurement and the reference is modulated via a wavelength scan instead of a mechanical scan. When the OPD is small, the modulation frequency is small, and conversely, the larger the OPD, the larger the modulation frequency. So the OPD can be specified by the modulation frequency of the interference fringe pattern. The wavelength swept range is 16 nm, from 765 nm to 781 nm and its corresponding linewidth is less than  $3.98 \times 10^{-7}$  nm. During the wavelength scan, the output power is controlled to stay constant without any abrupt changes via constant power mode operation. We obtain 160 interference fringe patterns for each subaperture measurement and the camera frame rate is 38 frames  $s^{-1}$ .

### 2.1. Basic principle of wavelength scanning interferometry

The interferogram intensity of the wavelength scanning interferometer can be described as [5]

$$\begin{aligned} I(x, y; k) &= a(x, y; k) + b(x, y; k) \cos[2(k - k_0)h(x, y) + 2k\Lambda] \\ &= a(x, y; k) + b(x, y; k) \cos[\Phi(x, y; k) + 2k\Lambda] \\ &= a(x, y; k) + c(x, y; k) e^{j2k\Lambda} + c(x, y; k)^* e^{-j2k\Lambda}, \quad (1) \end{aligned}$$

where  $a(x, y; k)$  and  $b(x, y; k)$  are the slow-varying spectral background and spectral fringe visibility at each pixel, respectively.  $c(x, y; k)$  is  $\frac{1}{2}b(x, y; k)e^{j\Phi(x, y; k)}$ ,  $k$  is the wavenumber defined as  $2\pi/\lambda$ ,  $k_0$  is the initial wavenumber defined as  $2\pi/\lambda_0$ ,  $\lambda$  and  $\lambda_0$  are the wavelength of source and the starting wavelength, respectively.  $\Lambda$  is the additional spectral carrier component induced by increasing the OPD between the reference and the target, and  $h(x, y)$  represents the target surface. In order to extract the phase of the interference signal,  $\Phi(x, y; k)$ , the Fourier transform technique is used. In general, as the OPD between the beams in the MIO increases, the fringe visibility gets worse. Here, the intensity of the interferogram is modulated by the spectral carrier frequency  $\Lambda$ , which is proportional to the OPD as the wavelength of the light source is tuned. To extract the phase of the interference signal via the Fourier transform technique, we need to obtain more than two cycles of a sinusoidal interference over the wavelength scan. So we adjust the OPD so as to get roughly three cycles of a sinusoidal interference. The Fourier transformed signal of  $I(x, y; k)$  can be expressed as

$$FT[I(x, y; k)] = A(x, y; f_k) + C(x, y; f_k - \Lambda) + C(x, y; f_k + \Lambda)^*, \quad (2)$$

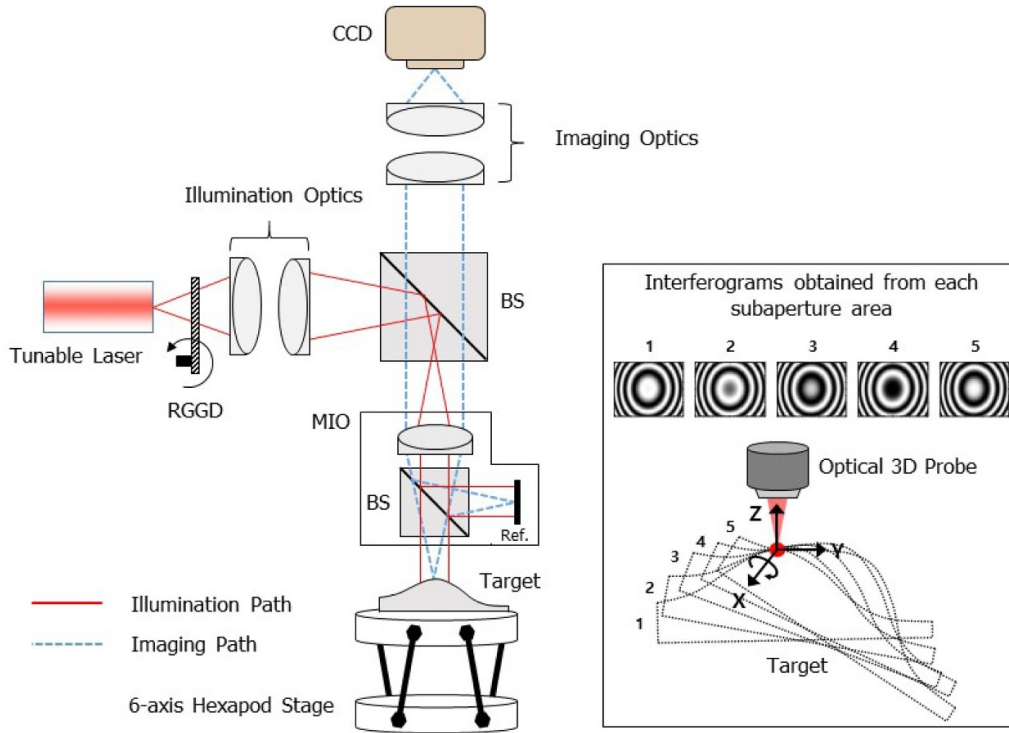


**Figure 1.** Schematic diagram of subaperture stitching wavelength scanning interferometry for 3D surface measurement of complex optics; TL: tunable laser, RGGD: rotating ground glass diffuser, BS: beam splitter, MIO: Michelson-type interference objectives, ref.: reference flat, CCD: charge coupled device.

where,  $A(x, y; f_k)$  and  $C(x, y; f_k)$  denote the Fourier transforms of  $a(x, y; k)$  and  $c(x, y; k)$ .  $C(x, y; f_k)$  and its complex conjugate  $C(x, y; f_k)^*$  are separated by the amount of  $\Lambda$  in the positive and negative domain, respectively. The phase information of  $\Phi(x, y; k)$  can be obtained through the double-Fourier transform method. After applying a suitable window filter such as the Hanning window into equation (2),  $C(x, y; f_k)$  can be selectively extracted. And then the inverse Fourier transform of  $C(x, y; f_k)$  gives

$$\begin{aligned} \text{FT}^{-1}[C(x, y; f_k)] &= \text{FT}^{-1} \text{FT} \left[ \frac{1}{2} b(x, y; k) e^{j\Phi(x, y; k)} \right] \\ &= \frac{1}{2} b(x, y; k) e^{j\Phi(x, y; k)}. \end{aligned} \quad (3)$$

Then,  $\Phi(x, y; k)$  can be extracted by taking the logarithmic function and finding the imaginary part sequentially

$$\begin{aligned} &\text{imag} \left[ \ln \left( \frac{1}{2} b(x, y; k) e^{j\Phi(x, y; k)} \right) \right] \\ &= \text{imag} \left[ \ln \left( \frac{1}{2} b(x, y; k) \right) + j\Phi(x, y; k) \right] = \Phi(x, y; k). \end{aligned} \quad (4)$$

Hence, the surface profile of the target can be calculated by the derivate of  $\Phi(x, y; k)$  with  $k$  as

$$h(x, y) = \frac{1}{2} \frac{\partial \Phi(x, y; k)}{\partial k}. \quad (5)$$

## 2.2. Subaperture stitching technique using multi-axis positioning stage

Interferometric measurement of freeform surfaces is still a challenge owing to too dense or invisible fringes. To overcome these problems, we propose a subaperture stitching technique using the high-accuracy multi-axis position stage. We keep the optical probe perpendicular to the surface slope during subaperture measurement by rotating and translating the target surface around a fixed pivot position. We selected a pivot position at an arbitrary point on the target surface and fixed it. Figure 2 shows how to control the target position in order to maintain the perpendicular geometrical relation between the probe and the surface slope for the subaperture measurement. This schematic diagram presents only the YZ plane, and it is similar to the XZ plane. First, we rotated the target around the pivot point until the probe was perpendicular to the measuring subaperture area. Here, the rotation angle can be calculated using the normal vector  $\hat{n}$  of subaperture area and  $\hat{n}$  can be easily obtained from the surface design value provided by a manufacturer. Next, we moved the target along the  $y$ - and  $z$ -directions for subaperture measurement with good visibility fringes.

As described above, each subaperture measurement is performed by maintaining the perpendicular relationship between the optical probe and the surface slope. During the subaperture measurement, a series of interference patterns with good visibility are continuously obtained by using a rotation matrix around the pivot point, and the rotation matrix can be derived

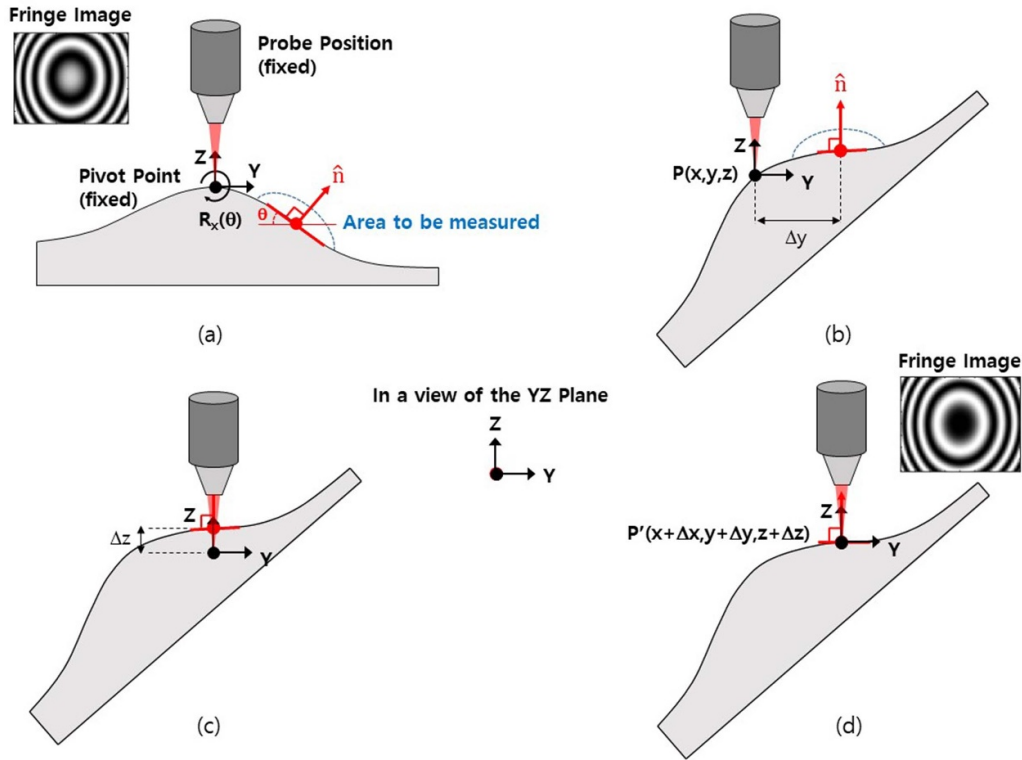


**Figure 2.** Subaperture measurement procedure described from the viewpoint of the YZ plane: calculation of (a) rotation angle  $R_x(\theta)$ , (b) Y-translation distance  $\Delta y$ , (c) Z-offset distance  $\Delta z$  from a fixed pivot position based on the surface normal vector to the area to be measured, and (d) setup ready for the next subaperture measurement after the measurement position is moved from  $P(x, y, z)$  to  $P'(x + \Delta x, y + \Delta y, z + \Delta z)$ .

from the surface shape equation in the Cartesian coordinate system.

$$F(x, y, z) = \text{constant, or } z = f(x, y). \quad (6)$$

The normal vector to the above surface is given by

$$\hat{n} = \nabla F(x, y, z) = \left( \frac{\partial F}{\partial x}, \frac{\partial F}{\partial y}, \frac{\partial F}{\partial z} \right) = (l, m, n). \quad (7)$$

Then, the direction cosines of the normal vector  $\hat{n}$  are

$$\begin{aligned} \alpha &= \cos \theta_x = \frac{l}{\sqrt{l^2 + m^2 + n^2}} \\ \beta &= \cos \theta_y = \frac{m}{\sqrt{l^2 + m^2 + n^2}} \\ \gamma &= \cos \theta_z = \frac{n}{\sqrt{l^2 + m^2 + n^2}}. \end{aligned} \quad (8)$$

Once the direction cosines are calculated, we can determine a  $4 \times 4$  rotation matrix in the YZ plane, expressed as

$$R_x(\theta_y) = \begin{pmatrix} 1 & 0 & 0 & 0 \\ 0 & \cos(90 - \theta_y) & -\sin(90 - \theta_y) & 0 \\ 0 & \sin(90 - \theta_y) & \cos(90 - \theta_y) & 0 \\ 0 & 0 & 0 & 1 \end{pmatrix}. \quad (9)$$

In a similar way, the rotation in the XZ plane can be calculated as

$$R_y(\theta_x) = \begin{pmatrix} \cos(90 - \theta_x) & 0 & \sin(90 - \theta_x) & 0 \\ 0 & 1 & 0 & 0 \\ -\sin(90 - \theta_x) & 0 & \cos(90 - \theta_x) & 0 \\ 0 & 0 & 0 & 1 \end{pmatrix}. \quad (10)$$

Then, when the sample is translated by  $\Delta x$  and  $\Delta y$  in the x and y directions, the offset distance  $\Delta z$  and its corresponding translation matrix can be calculated as

$$T(\Delta x, \Delta y, \Delta z) = \begin{pmatrix} 1 & 0 & 0 & \Delta x \\ 0 & 1 & 0 & \Delta y \\ 0 & 0 & 1 & \Delta z \\ 0 & 0 & 0 & 1 \end{pmatrix}, \quad (11)$$

$$\Delta z = f(x + \Delta x, y + \Delta y) - f(x, y).$$

Using equations (9)–(11), we can combine these 3D transform matrices to represent complicated transformations with a single transform matrix, as follows:

$$M(\Delta x, \Delta y, \Delta z, \theta_x, \theta_y) = T(\Delta x, \Delta y, \Delta z) R_y(\theta_x) R_x(\theta_y). \quad (12)$$

So the next subaperture measurement position  $P'(x + \Delta x, y + \Delta y, z + \Delta z)$  can be calculated from the previous measurement position  $P(x, y, z)$

$$P'(x + \Delta x, y + \Delta y, z + \Delta z) = M(\Delta x, \Delta y, \Delta z, \theta_x, \theta_y) P(x, y, z). \quad (13)$$

Hence, we can keep the optical probe perpendicular to the surface slope in order to obtain good visibility fringes during measurement using the 3D transform matrix from equation (13). By doing this, we can extend the effective aperture and dynamic range by stitching many subapertures of the surface together to synthesize a full aperture map. As shown in

figure 3, we can obtain good quality interference images at each subaperture measurement. So the full coverage, even on complex-shaped parts, is possible. Because the relative position of each subaperture measurement is not known exactly due to stage motion errors, there are some measurement errors when synthesizing a full aperture map from a series of overlapped subaperture maps. We used a six-axis stage to allow precise positioning with nanometer resolution and a six DOF (degree-of-freedom) stitching method was implemented to compensate the unexpected uncertainty errors that occurred during the stitching process.

Typically, a stitching method is based on matching three parameters (3 DOF) of planes representing height maps between the overlapped areas of adjacent subaperture measurement results. In this case, the plane can be defined as

$$z = ax + by + c, \quad (14)$$

where  $a$  and  $b$  are the slopes of the plane along  $x$  and  $y$  axes, respectively, and  $c$  is the height offset. Then, the overlapping region between two adjacent planes ( $m$ - and  $n$ - planes) can be described as

$$\begin{aligned} z_{m,n} &= a_{m,n}x + b_{m,n}y + c_{m,n}, \\ z_{n,m} &= a_{n,m}x + b_{n,m}y + c_{n,m}. \end{aligned} \quad (15)$$

The subscription ( $m, n$ ) means the parameters of the  $m$ -plane in the region overlapping with the  $n$ -plane, and ( $n, m$ ) is *vice versa*. For successful stitching, the slopes and the offsets of  $z_{m,n}$  and  $z_{n,m}$  should be the same, which means they should be adjusted in one of the planes. With the operation of matching the planes in the overlapping region, the whole height map can be reconstructed from the subaperture measurement results.

However, the most important issue in this three DOF stitching method is the lateral coordinate of ( $x, y$ ) which should be precisely determined. If the ( $x, y$ ) errors including the axial rotation ( $\theta_z$ ) are involved in the measurement result, the whole height map can be distorted. To overcome this limitation, in this investigation the six DOF stitching method to compensate the lateral position and axial rotation errors is applied with an iterative procedure. First of all, the overlapping region based on the adjacent measurement results is determined, and the corresponding planes ( $z_{m,n}$  and  $z_{n,m}$ ) are adjusted with the three DOF stitching method as the same. Then, the height maps of  $z_{m,n}$  and  $z_{n,m}$  are compared with each other, and the best lateral positions are determined based on optimization with the following objective function.

$$F(\Delta x, \Delta y, \Delta \theta_z) = \sum [H_{m,n}(x, y, \theta_z) - H_{n,m}(x + \Delta x, y + \Delta y, \theta_z + \Delta \theta_z)]^2. \quad (16)$$

where  $H$  represents the height map corresponding to the plane  $z$ .  $\Delta x$ ,  $\Delta y$ , and  $\Delta \theta_z$  are the lateral positions and axial rotation changes. After the lateral positions of the subaperture height maps are calibrated, the three DOF stitching method is applied to the calibrated height maps, and the whole height map can be reconstructed.

Figure 4 shows a performance comparison of the three DOF and six DOF stitching methods. In case the positioning errors are included in each subaperture measurement, the specific points in the height map reconstructed by the three DOF method are blurred and misaligned, but they are exactly stitched and well aligned with each other by the six DOF method.

Generally, the overlapping ratio between two adjacent subapertures needs to be set larger than 30% for the stitching method [22]. In this paper, we obtained subaperture height maps with an overlapping ratio of approximately 30%.

### 3. Experimental results

We measured several representative samples to verify the optical performance of our proposed system. Before measurement, the optical system was calibrated by comparing the measurement value performed by our system in tests with step-height standards of known accuracy. Then, measurements were performed on various test samples, such as spherical, aspherical, and parabolic surfaces to verify the system performance in comparison with a well-known stylus profiler. Table 1 shows the system specification used in this investigation, and details about the system calibration and verification are described as follows.

#### 3.1. Step-height standards measurement for system calibration

We used a NIST traceable step height standard (SHS-880QC by VLSI Standards Inc.) to calibrate our proposed system. This step-height specimen has a nominal value of 88.7 nm with a standard uncertainty of 1.3 nm. We measured the step-height standards 10 times and the average height was 88.9 nm with a standard deviation of 1.74 nm. The step height measurement result by our proposed method was well matched to the certified height value. Measuring a step height does not give us a guarantee for the measurement of complex surfaces, and the uncertainty evaluation for surface measurement is very complicated [25]. In this paper, we only considered the contribution of the repeatability to uncertainty and measured several representative samples including spherical, aspherical, even parabolic off-axis mirrors to demonstrate the measurement ability for complex surfaces.

#### 3.2. Various sample measurements for verification of system performance

Our proposed method was verified by measuring several representative samples from spherical and aspherical surfaces to even off-axis parabolic surfaces, and we compared our measurement results with those of a commercial profilometer (UA3P-5). We also extended the effective aperture and dynamic range of the wavelength scanning interferometry by combining and stitching the individual subaperture data sets for a synthesized large-aperture measurement. The general shape equation for a lens surface can be expressed as

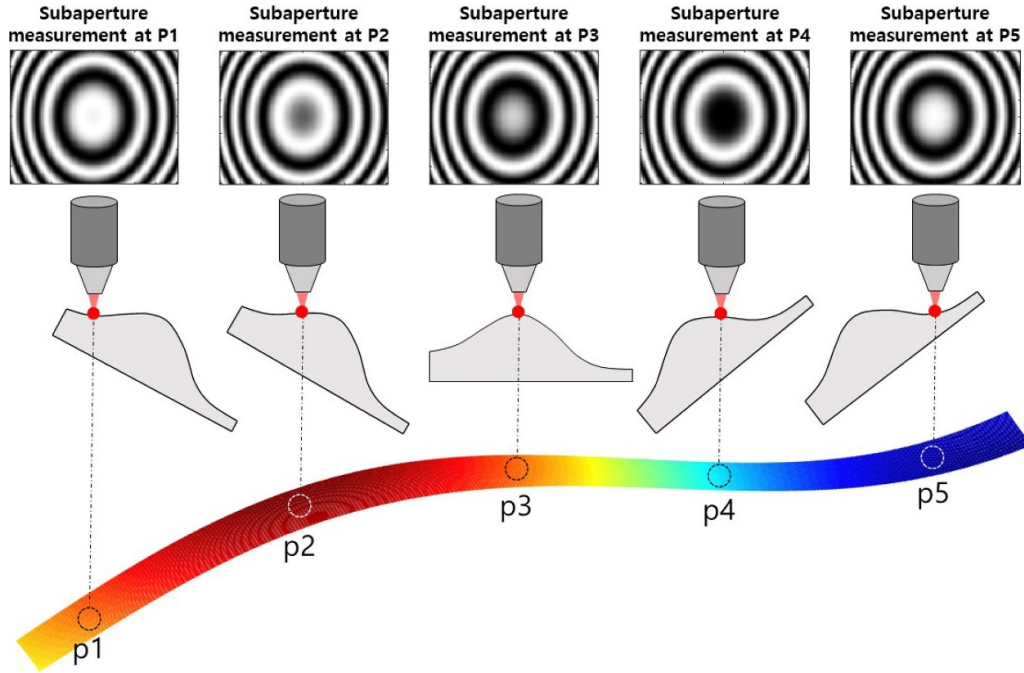


**Figure 3.** Subaperture stitching technique for extending the effective aperture and dynamic range.

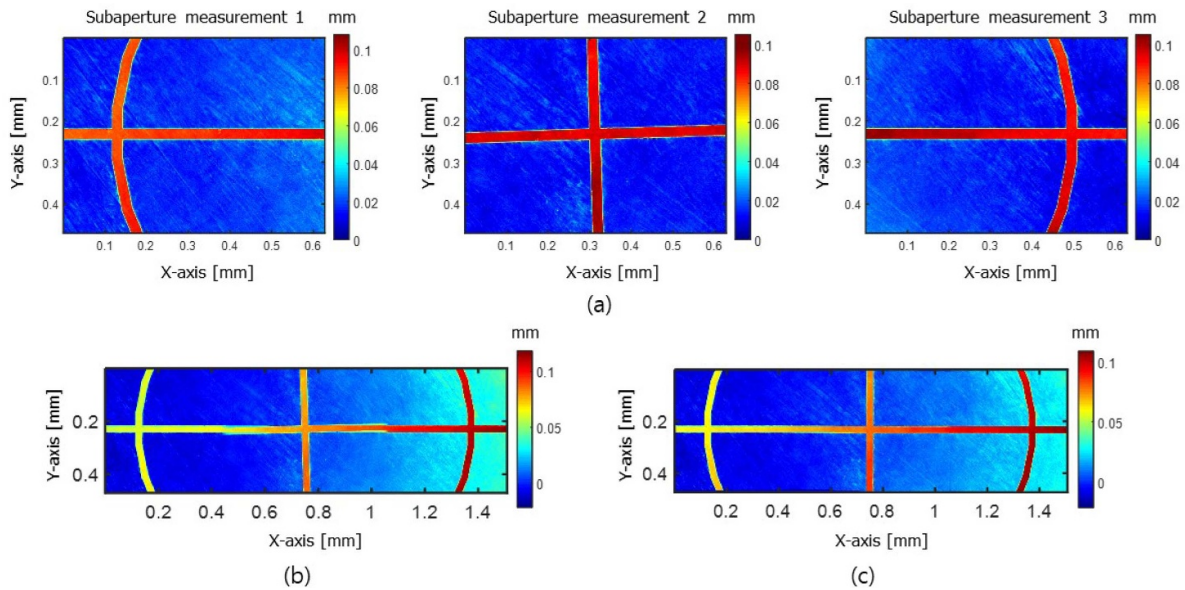


**Figure 4.** Comparison of three DOF and six DOF stitching methods: (a) subaperture measurement results when the positioning errors are included, (b) reconstructed whole height map of (a) with three DOF stitching method, and (c) reconstructed whole height map of (a) with six DOF stitching method.

$$z = \frac{Cr^2}{1 + \sqrt{1 - (1 + K)C^2r^2}} + A_4r^4 + A_6r^6 + A_8r^8 + \dots + A_i r^i, \tag{17}$$

where  $C$  denotes the curvature of the surface,  $r$  is the radial distance from the optical axis,  $K$  is a constant called conic coefficient. Depending on the conic coefficient, the lens shape differs. For example,  $K = 0$  means a spherical surface,  $K = -1$  is a parabolic surface,  $K > 0$  or  $-1 < K < 0$  means ellipsoid, and finally  $K < -1$  means a hyperbolic surface.  $A_i$  is the  $i$ th

aspheric coefficient, which means the degree of deviation from the conical surface.

Figure 5 shows the measurement result of an aspheric mirror where the radius of curvature at the aspheric equation was  $R = 51.95$  mm, conic coefficient  $K = 2.309$ , aspherical coefficients  $A_i = 0$ . As shown in figure 5(a), we acquired the extended full aperture area by stitching the data sets of 72 local regions of the aspherical shape, while the measurement probe was kept perpendicular to the measurement region. After obtaining the stitched full aperture map, the radius of

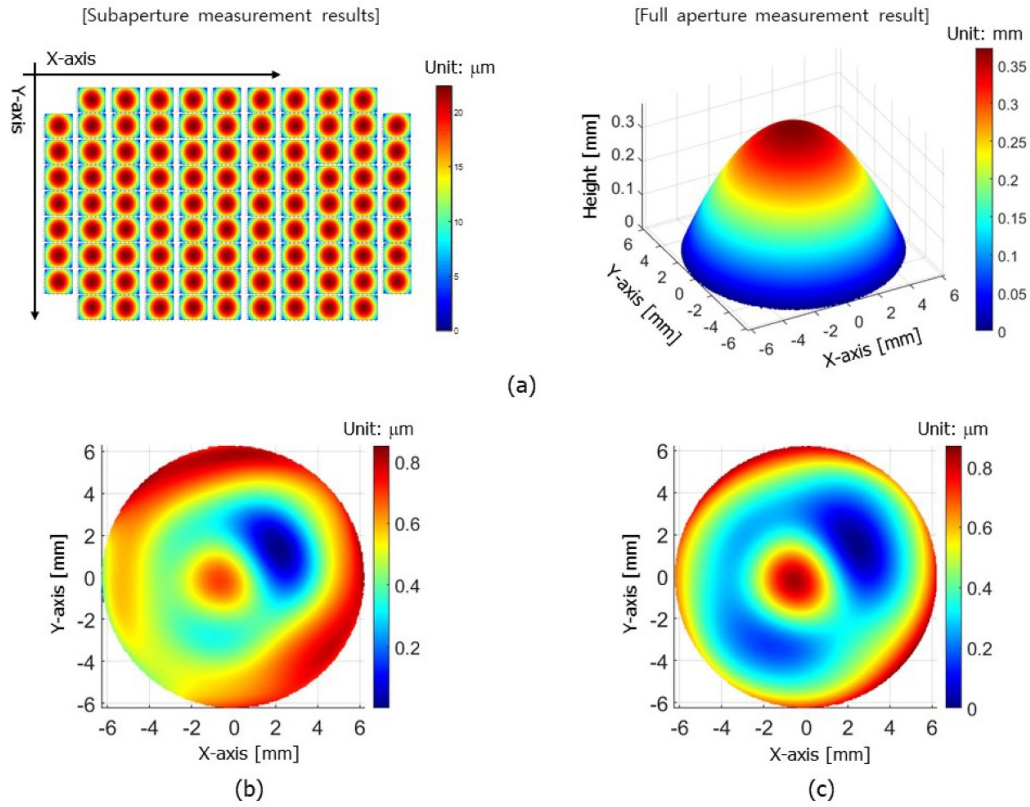


**Figure 5.** Measurement results of a convex aspheric lens surface: (a) reconstructed 3D surface profile after stitching subaperture measurement results and the residual error map of (b) our proposed method and (c) the UA3P-5 method after subtracting a best-fit model.

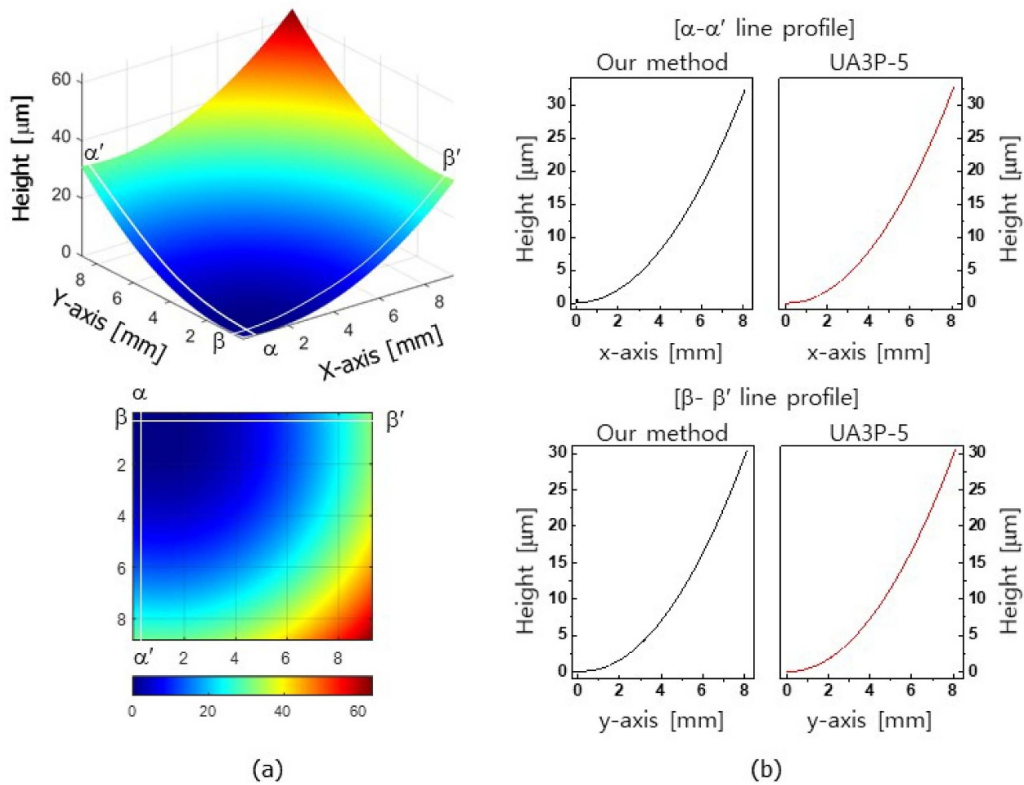


**Figure 6.** Measurement results of an off-axis parabolic mirror surface: (a) reconstructed 3D surface profile using our proposed method and (b) comparisons of our measurement results with those of the UA3P-5 method.

**Table 1.** Specifications of the optical system used for experiments.

Item	Specification
Wavelength tuning range	765 nm to 781 nm
Interference objectives	5 magnification with 0.13 N.A.
Six-axis hexapod stage	Travel range $X(\pm 17 \text{ mm}), Y(\pm 16 \text{ mm}), Z(\pm 6.5 \text{ mm}), \theta_x(\pm 10^\circ), \theta_y(\pm 10^\circ), \theta_z(\pm 21^\circ)$
	Repeatability (RMS, $\pm 1\sigma$ ) $X(\pm 150 \text{ nm}), Y(\pm 150 \text{ nm}), Z(\pm 60 \text{ nm}), \theta_x(\pm 2 \mu\text{rad}), \theta_y(\pm 2 \mu\text{rad}), \theta_z(\pm 3 \mu\text{rad})$
Field of view (subaperture)	1.13 mm $\times$ 0.952 mm
Camera resolution	1024 $\times$ 1224

**Table 2.** Comparisons between our method and a commercial instrument.

Coefficients of lens surface	Radius of curvature $R$	
	Our method ( $\pm 1\sigma$ )	UA3P-5
$R = 51.95 \text{ mm}, K = 2.309$	$52.38 \pm 0.01 \text{ mm}$	52.19 mm
$R = 100 \text{ mm}, K = 0$	$100.41 \pm 0.01 \text{ mm}$	99.96 mm
$R = 150 \text{ mm}, K = 0$	$150.52 \pm 0.01 \text{ mm}$	150.18 mm
$R = 200 \text{ mm}, K = 0$	$200.86 \pm 0.01 \text{ mm}$	199.94 mm

curvature was measured to be 52.38 mm by fitting the aspherical model of equation (17) into the synthesized full aperture measurement result. Figures 5(b) and (c) show the residual error maps corresponding to our method and the UA3P-5 commercial instrument after subtracting a best-fit model, respectively. These resultant residual error maps show similar trends where a PV of our method was 0.859  $\mu\text{m}$  and that of UA3P-5 was 0.874  $\mu\text{m}$ .

To evaluate the performance of our proposed technique, we repeatedly performed the measurement for each subaperture 10 times. The repeatability of all individual subaperture measurements is less than 24 nm because the stability of the interferogram is guaranteed during the subaperture measurement. Also, the radii of curvature of each sample were repeatedly measured 10 times and we indicated the repeatability of each measurement result. The data acquisition time for each subaperture is less than 5 s and the measurement and calculation time for 72 subapertures is nearly 23 min. Table 2 summarizes the measurement results compared with reference data from UA3P-5.

As shown in table 2, the measured values of our method are consistent with those of the UA3P-5 for spherical and aspherical surfaces with various radii of curvature.

Next, we measured an off-axis parabolic mirror surface as a representative example of a freeform surface and a 3D surface profile map was reconstructed by stitching 100 overlapped subaperture data maps. The data acquisition time for each subaperture is less than 5 s and the measurement and calculation time for 100 subapertures is about 30 min. Figure 6 shows the full-aperture stitch result and its comparison results with UA3P-5 method. The comparisons of the two methods at the  $\alpha\text{-}\alpha'$  and  $\beta\text{-}\beta'$  lines show that our measurement results are well matched to the UA3P-5 results and the maximum

deviation between these two results is estimated to be less than 0.43  $\mu\text{m}$ .

#### 4. Conclusion

In summary, we propose a new scheme of subaperture stitching wavelength scanning interferometry for the complete coverage of complex-shaped optics. To obtain good fringe visibility, each subaperture measurement is performed while keeping the optical probe perpendicular to the surface slope and the position of the sample in the XYZ coordinate is calculated using a 3D transformation matrix. We rotate and translate the sample around a well-defined pivot point using a six-axis positioning stage with nanometer precision. Also, a six DOF stitching technique is used to minimize stitching errors. To verify our proposed method, we measured several representative examples of spherical, aspherical, and parabolic surfaces and compared the measurement results with a commercial tactile UA3P instrument. The difference between the measurements using the two methods was small, and the comparison results matched each other well. We anticipate that our proposed subaperture stitching wavelength scanning interferometry can be an alternative tool for 3D measurements of complex-shaped optics, such as freeform surfaces.

#### Acknowledgments

This research was supported by the Commercialization Promotion Agency for R&D Outcomes (COMPA), 'Real-time 3D surface measurement for aspheric and freeform lens', funded by the Ministry of Science and ICT (MSIT).

#### ORCID iDs

Ki-Nam Joo  <https://orcid.org/0000-0001-9484-2644>

Young-Sik Ghim  <https://orcid.org/0000-0002-4052-4939>

#### References

- [1] Fang F Z, Zhang X D, Weckenmann A, Zhang G X and Evans C 2013 Manufacturing and measurement of freeform optics *CIRP Ann.* **62** 823–46
- [2] Hu X and Hua H 2014 High-resolution optical see-through multi-focal-plane head-mounted display using freeform optics *Opt. Express* **22** 13896–903

- [3] Tsutsumi H, Yoshizumi K and Takeuchi H 2005 Ultrahighly accurate 3D profilometer *Proc. SPIE* **5638** 387–94
- [4] Wyant J C 1973 Double frequency grating lateral shearing interferometer *Appl. Opt.* **12** 2057–60
- [5] Ghim Y-S, Rhee H-G, Davies A, Yang H-S and Lee Y-W 2014 3D surface mapping of freeform optics using wavelength scanning lateral shearing interferometry *Opt. Express* **22** 5098–105
- [6] Knauer M C, Kaminski J and Häusler G 2004 Phase measuring deflectometry: a new approach to measure specular free-form surfaces *Proc. SPIE* **5457** 366–76
- [7] Nguyen M T, Ghim Y-S and Rhee H-G 2019 Single-shot deflectometry for dynamic 3D surface profile measurement by modified spatial-carrier frequency phase-shifting method *Sci. Rep.* **9** 3157
- [8] Southwell W H 1980 Wave-front estimation from wave-front slope measurements *J. Opt. Soc. Am.* **70** 998–1006
- [9] Phuc P H, Nguyen M T, Rhee H-G, Ghim Y-S, Yang H-S and Lee Y-W 2017 Improved wavefront reconstruction algorithm from slope measurements *J. Korean Phys. Soc.* **70** 469–74
- [10] Hariharan P, Oreb B F and Eiju T 1987 Digital phase-shifting interferometry: a simple error-compensating phase calculation algorithm *Appl. Opt.* **26** 2504–6
- [11] Han G-W and Kim S-W 1994 Numerical correction of reference phases in phase-shifting interferometry by iterative least-squares fitting *Appl. Opt.* **33** 7321–5
- [12] Gao P, Yao B, Lindlein N, Mantel K, Harder I and Geist E 2009 Phase-shift extraction for generalized phase-shifting interferometry *Opt. Lett.* **34** 3553–5
- [13] Harasaki A, Schmit J and Wyant J C 2000 Improved vertical-scanning interferometry *Appl. Opt.* **39** 2107–15
- [14] Gao F, Leach R K, Petzing J and Coupland J M 2008 Surface measurement errors using commercial scanning white light interferometers *Meas. Sci. Technol.* **19** 015303
- [15] Ghim Y-S and Davies A 2012 Complete fringe order determination in scanning white-light interferometry using a Fourier-based technique *Appl. Opt.* **51** 1922–8
- [16] Xue S, Chen S, Fan Z and Zhai D 2018 Adaptive wavefront interferometry for unknown free-form surface *Opt. Express* **26** 21910–28
- [17] Weg C W, Berger G, May T, Nicolaus R and Petter J 2014 Method and device for measuring surfaces in a highly precise manner U.S. patent 8736850 B2
- [18] Henselmans R, Cacace L A, Kramer G F Y, Rosielle P C J N and Steinbuch M 2011 The NANOMEFOS non-contact measurement machine for freeform optics *Precis. Eng.* **35** 607–24
- [19] Jiang X, Wang K, Gao F and Muhamedsalih H 2010 Fast surface measurement using wavelength scanning interferometry with compensation of environmental noise *Appl. Opt.* **49** 2903–9
- [20] Ghim Y-S, Suratkar A and Davies A 2010 Reflectometry-based wavelength scanning interferometry for thickness measurements of very thin wafers *Opt. Express* **18** 6522–9
- [21] Yamaguchi I J, Yamamoto A and Yano M 2000 Surface topography by wavelength scanning interferometry *Opt. Eng.* **39** 40–46
- [22] Bray M 1997 Stitching interferometer for large plano optics using a standard interferometer *Proc. SPIE* **3134** 39–50
- [23] Murphy P, Forbes G, Fleig J, Dumas P and Tricard M 2003 Stitching interferometry: a flexible solution for surface metrology *Opt. Photon. News* **14** 38–43
- [24] Chen S, Xue S, Dai Y and Li S 2015 Subaperture stitching test of large steep convex sphere *Opt. Express* **23** 29047–58
- [25] Leach R K 2015 Is one step height enough? *Proc. ASPE* 110–3